Molecular Vision 2022; 28:394-411 <http://www.molvis.org/molvis/v28/394>
Received 10 June 2022 | Accepted 11 November 2022 | Published 12 November 2022

Morphological, biochemical, and transcriptomic characterization of iPSC-derived human RPE cells from normal and Smith-Lemli-Opitz syndrome patients

Michael H. Farkas,[1,2,3] Lara A. Skelton,[1,2,3] Sriganesh Ramachandra-Rao,[1,2,3] Elizabeth Au,[1] Steven J. Fliesler[1,2,3]

(The first three authors have contributed equally to this work.)

[1]Department of Ophthalmology (Ross Eye Institute), The State University of New York- University at Buffalo, Buffalo, NY; [2]Department of Biochemistry and the Neuroscience Graduate Program, The State University of New York- University at Buffalo, Buffalo, NY; [3]Research Service, VA Western New York Healthcare System, Buffalo, NY

Purpose: Smith-Lemli-Opitz syndrome (SLOS) is a human recessive disease that affects cellular cholesterol (Chol) synthesis due to mutations in the gene encoding 7-dehydrocholesterol-reductase (DHCR7), resulting in defective reduction of 7-dehydrocholesterol (7-DHC) to Chol. Genetic and pharmacological rodent models of SLOS reveal progressive retinal and retinal pigmented epithelium (RPE) pathology. In this study, we aimed to characterize *in vitro* models of human RPE SLOS pathology utilizing two SLOS patient-derived induced pluripotent stem cell-derived RPE (iPSC-RPE) cell lines—"mild" SLOS (CWI) and "severe" SLOS (A2)—versus a normal human iPSC-RPE cell line (DYS) and performed comparative transcriptomic, morphological, and biochemical analyses.

Methods: iPSC-derived RPE cultures were differentiated and matured in parallel for 2.5 months and monitored by brightfield microscopy. *DHCR7* mutations were verified by PCR amplification spanning the target region and sequencing. Total RNA was isolated from replicate cultures, and RNA-Seq libraries were prepared and sequenced. Whole cell lysates were prepared from parallel cultures and subjected to Western blot analysis to assess the expression levels of RPE-specific and differentiation markers. Each RPE cell line was analyzed by confocal microscopic immunohistochemistry to further assess morphology, cell border integrity (zona occludens/tight junction protein-1 (TJP-1) and occludin), and F-actin distribution and organization (fluor-conjugated phalloidin). Sterol profiling (by reverse-phase HPLC analysis) was performed on similarly matured cultures that were switched to delipidated (Chol-free) media for 9 days prior to analysis.

Results: RNA-Seq libraries from the RPE cell lines showed a comparable number of total isoforms. Inter-sample concordance was high between A2-SLOS versus Dys0100 RPE (0.90) but was low when comparing CWI-SLOS versus Dys0100 RPE (0.78), or A2-SLOS versus CWI-SLOS RPE (0.65). Out of the 86 RPE markers analyzed, 82 were expressed in A2-SLOS RPE, whereas 85 were expressed in both CWI-SLOS and Dys0100 RPE. Inter-sample concordance for RPE markers was high for CWI-SLOS versus Dys0100 RPE cells (0.92) but low between A2-SLOS versus Dys0100 (0.13) and A2-SLOS versus CWI-SLOS (0.05). Upregulation of transcripts for epithelial-to-mesenchymal transition markers and downregulation of RPE-specific markers were observed in both SLOS iPSC-RPE cell lines, in agreement with Western blot results that revealed elevated expression of smooth muscle actin in SLOS-derived RPE cell lines. CWI and A2 RPE cells exhibited altered monolayer organization, marked stress fiber formation, and aberrant TJP1 and occludin labeling patterns. Sterol analysis demonstrated a significantly elevated 7DHC/Chol mol ratio in A2 RPE cells compared to CWI and DYS RPE cells. Both the A2 and CWI RPE cells were responsive to Chol depletion and exhibited lipid droplet accumulation.

Conclusion: Our data demonstrate DHCR7 mutation-dependent accumulation of 7DHC and lipid droplets, as well as altered RPE marker expression in SLOS iPSC-derived RPE cell lines. The degree of the observed abnormalities correlated with disease severity. These cell lines represent a novel biological resource for studies aimed at further understanding

Correspondence to: Steven J. Fliesler, Research Service-VAWNYHS, 3495 Bailey Avenue- Mail Stop 151, Buffalo, NY, 14215-1129; Phone: 716-862-6538; FAX: 716-862-6526; email: fliesler@buffalo.edu

the pathobiology of SLOS, particularly as it involves SLOS-associated visual system dysfunction, and for *in vitro* testing of candidate therapeutic drugs or gene therapy approaches to improve clinical management of SLOS patients.

Smith-Lemli-Opitz syndrome (SLOS; OMIM 270400) is an autosomal recessive congenital syndrome with an estimated incidence of 1 in 20,000–60,000 live births [1,2]. SLOS clinical features lack phenotype–genotype correlation [3] and involve 2–3 toe syndactyly and craniofacial abnormalities, as well as skin heart, urogenital, and vision-associated pathology [2]. SLOS is caused by loss-of-function mutations in the gene coding for sterol Δ7-reductase (7-dehydrocholesterol reductase, *DHCR7*; EC 1.3.1.21; chromosome 11q13.4; OMIM 602858) [4,5]. DHCR7 catalyzes the ultimate step in the Kandutsch–Russell sterol synthesis pathway—the conversion of 7-dehydrocholesterol (7DHC) to cholesterol (Chol)—via reduction of the Δ7 double bond in ring B of the sterol nucleus of 7DHC [5]. SLOS-associated *DHCR7* mutations elevate the molar ratio of the 7DHC/Chol in all tissues and fluids (compared to normal extremely low or negligible levels of 7DHC).

Of the approximately 150 known *DHCR7* mutations, the IVS8–1G>C splice site mutation is the most common, which most often leads to a moderate-to-severe form of SLOS, while the T93M mutation is the most common missense mutation [1-3,6]. Severely affected individuals have numerous congenital dysmorphologies, and typically die shortly after birth, if not in utero [7]. By comparison, SLOS individuals with mild to moderate morphological and cognitive defects (e.g., hypomorphic T93M *DHCR7* homozygous mutation) nonetheless exhibit distinct behavioral abnormalities consistent with autism spectrum disorders [2,8,9]. Although no definitive ocular phenotype has been ascribed to SLOS, visual dysfunction has been reported in clinically diagnosed SLOS patients. Significantly reduced rod electroretinogram response amplitudes, with reduced activation and inactivation kinetics, have been reported [10]. However, cone electroretinogram responses have not been found to be significantly altered [11]. Unfortunately, the extant literature pertaining to SLOS patients is lacking with regard to retinal structure information, for example, obtained either in vivo by spectral domain optical coherence tomography (SD-OCT) or from postmortem retinal histopathology analysis [12]. To date, the mechanisms underlying SLOS-associated retinal dysfunction, including the possible involvement of retinal pigmented epithelium (RPE) pathology, remain unknown.

The role of RPE pathology in SLOS-associated retinal dysfunction remains to be investigated. Animal models of SLOS have been developed, either via genetic modification approaches [13-15] or pharmacological inhibition of DHCR7 in rodents [16-18]. We previously demonstrated progressive, irreversible, photoreceptor-specific retinal degeneration in rats treated with the DHCR7 inhibitor AY9944 [18], in addition to the expected signature alterations in the sterol profiles of the retina, liver, brain, and serum compared to age- and sex-matched untreated control rats. The retinopathy observed in the SLOS animal model is accompanied by marked RPE pathology, characterized by congestion with undigested phagosomes derived from phagocytosis of the shed tips of the photoreceptor outer segments, altered basal infoldings, and lipid droplet accumulation [18,19]. To understand the mechanism of this RPE pathology, we have developed induced pluripotent stem cell (iPSCs)-derived RPE (iPSC-RPE) using fibroblasts isolated from SLOS patients and from an approximately age-matched normal human donor [19]. The strategy described herein involves the use of iPSC-RPE cells derived from a patient exhibiting a “mild” pathological phenotype, harboring both the *DHCR7* T93M and the IVS8–1G>C splice site mutations [20], that is, a compound heterozygote (designated “CWI” RPE cells). We also obtained iPSC-RPE cells derived from a SLOS patient exhibiting a “severe” phenotype, homozygous for the intron-exon junction IVS8G-C *DHCR7* mutation [20]; these were designated “A2” RPE cells.

In the present study, we investigated the morphological and protein biomarker features of CWI and A2 iPSC-RPE cells in comparison to normal human patient-derived iPSC-RPE cells (designated “DYS” RPE cells) as a control. We also compared the steady-state sterol composition of all three cultured cell lines, with a focus on the levels of 7DHC and Chol, as a function of the presence of normal (Chol-containing) serum versus delipidated (essentially Chol-free) serum in the culture medium. We then pursued a comparative transcriptomic analysis of all three iPSC-RPE cell lines to assess whether specific molecular signatures could explain the observed phenotypic differences.

METHODS

Basal media and antibodies: Basal culture media and serum were Dulbecco’s modified Eagle medium (DMEM) with HEPES (D6171, Millipore Sigma, Burlington, MA), DMEM without calcium chloride (21,068,028, Thermo Fisher Scientific, Grand Island, NY). KBM-Gold™ (192,151, keratinocyte basal medium, calcium ion-free; Lonza, Basel, Switzerland) and bovine calf serum (SH30073, HyClone Laboratories Inc., Logan, UT). Antibody and concentrations for Western blotting were anti-BEST1 (bestrophin) rabbit polyclonal at 1:1000 (LAgen laboratories, Rochester, MN); anti-CRALBP (cellular retinaldehyde binding protein) rabbit polyclonal

(1:1000, 15,356, Proteintech, Rosemont, IL); anti-RPE65 rabbit polyclonal (1:1000, GTX103472, Genetex, Irvine, CA); anti-β-actin mouse monoclonal (1:2000, 8H10D10, Cell Signaling Technology (CST), Danvers, MA); anti-ezrin (1:1000, 3145, CST); anti-vimentin (1:1000, ab92547 clone EPR3776, Abcam, Cambridge, MA), anti-E-cadherin monoclonal G10, (1:1000, sc-8426, Santa Cruz, Santa Cruz, CA), anti-α-tubulin (TUBA1) monoclonal, clone DM1A, (1:2000, T6199, Millipore Sigma); anti-α-smooth muscle actin (SMA) rabbit polyclonal (1:1000, ab5694, Abcam). Secondary alkaline phosphatase conjugated antibodies were obtained from Millipore Sigma: goat anti-rabbit IgG (A9919, 1:10,000) and goat anti-mouse IgG (AP124A, 1:10,000). For immunohistochemistry, we used anti-occludin monoclonal clone OC3-F10 (1:100, 33–1500, Thermo Fisher Scientific), anti-CRALBP clone B2, (1:100, NB100–74392, Novus Biologicals, Centennial, CO), anti-zonula occludens-1 [a.k.a. tight junction protein-1, TJP1] rabbit mAb D6L1E (1:100, 13,663, CST), fibronectin rabbit mAb E5H6X, (1:200, 26,836, CST), and a phalloidin-Alexa Fluor 568 conjugate to detect F-actin (1:500, OD044-T, Biotium, Freemont, CA).

RPE cell lines and culture conditions: Human iPSC-derived RPE cells originating from skin fibroblasts obtained initially from a "mildly" (CWI)-affected 6-month-old female, as well as from a normal neonatal male patient (Dys0100, DYS; ATCC, cat #ACS1019), were generated as described in detail previously [19]. Herein, we have further extended the analysis by including a "severe" SLOS phenotype. Briefly, A2 SLOS iPSC Clone 3F#1 was used at passage 17, and CWI SLOS iPSC Clone 4F#5 was used at passage 23 [20] for generating CWI and A2 SLOS iPSC-derived RPE cells (Neural Stem Cell Institute, New York, USA). The iPSC-derived RPE cells were then further passaged until P5–P6 (as described below) and used for further experimentation. We reconfirmed the SLOS genotypes in the CWI and A2 SLOS iPSC-RPE cells by PCR from isolated genomic DNA and direct sequence analysis (Figure 1E). Genomic DNA isolated from ARPE-19 cells (ATCC, cat#CRL2302), a commonly used transformed RPE cell line, was included as a control.

Passages 5–6 non-immortalized iPSC-RPE cells were seeded in 12-well tissue culture dishes (TCP011012, JET biofil, Elgin, IL USA) coated with a poly-L-ornithine solution (at 5 ug/cm^2; P4957, Millipore Sigma) at full confluence (~400,000 cells/well) and maintained at 37 °C under 6% CO_2-air atmosphere at 80% humidity. Conditions for the culture of iPSC-derived RPE cells were as described previously [19,21], with "high-calcium" and "low-calcium" media preparation and supplement formulation and addition, as described and enumerated previously in detail [22,23]. Briefly, we seeded and passaged the cells in "low-calcium" medium precluding the formation of calcium dependent adhesions to form a loosely bound, budding monolayer (DMEM plus calcium-free, keratinocyte basal medium, supplemented with growth factors and hormones, plus 1% (v/v) bovine calf serum (BCS) and 0.5% bovine retina extract (BRE)), prepared as described previously [21]. Cells were then switched after culturing for 3–7 days to defined "high-calcium" media (with supplements and 0.9% (v/v) BCS, and 0.25% (v/v) BRE), enabling synchronized cell–cell adhesion formation and promoting optimal differentiation with subsequent maturation of iPSC-RPE cells in culture [21,24]. All three iPSC-RPE cell lines were maintained in the presence of Plasmocin™ (ANTMPT, InvivoGen, San Diego, CA, at 37.5 µg/ml initial concentration, with 12.5 µg/ml maintenance dosage) to ensure the cultures were cleared and free of mycoplasma contamination, and were routinely verified using a commercial mycoplasma detection and removal kit (B39032, Bimake.com; Houston, TX). The iPSC-RPE monolayers were maintained in a "high-calcium" culture medium for at least two months before use. For routine inspection and imaging, cell cultures were inspected using an Axiovert 25 CFL inverted photomicroscope (Carl Zeiss Microscopy LLC, Thornwood, NY), equipped with an Evolution™ MP digital CCD 5.0 MP camera (MediaCybernetics, Rockville, MD). Digital images were captured and stored as .tiff files on a standard PC computer.

For experiments where the steady-state sterol composition (see below) of cells was assessed, the iPSC-RPE cell cultures were maintained as follows. Mature cellular monolayers cultured on 24-well plates were initially seeded and grown in 0.9% (v/v) BCS-containing "high-calcium" medium for about 3 months (see above), and were then transferred to "high-calcium" medium containing 0.9% (v/v) delipidated (sterol-depleted) calf serum (DLCS). The latter was prepared as previously described [25], and Chol depletion was verified to be >98% [19]. The final medium preparation excluded BRE supplementation. In parallel, cells maintained in a 0.9% BCS-containing medium were analyzed for sterol content. Prior to harvesting the cells for sterol analysis, the monolayers were washed three times in sterile PBS.

Immunohistochemical (IHC) analysis: For imaging by confocal fluorescence microscopy, iPSC-RPE cells were seeded in "low-calcium" medium on alcohol/UV-sterilized Rinzl plastic coverslips (72,261-22, Electron Microscopy Services (EMS), Hatfield, PA), coated with polyornithine solution (5 µg/cm^2), and switched after 2–7 days of culture to "high-calcium" medium to promote the formation of maturing polygonal iPSC-RPE cell monolayers. The cells

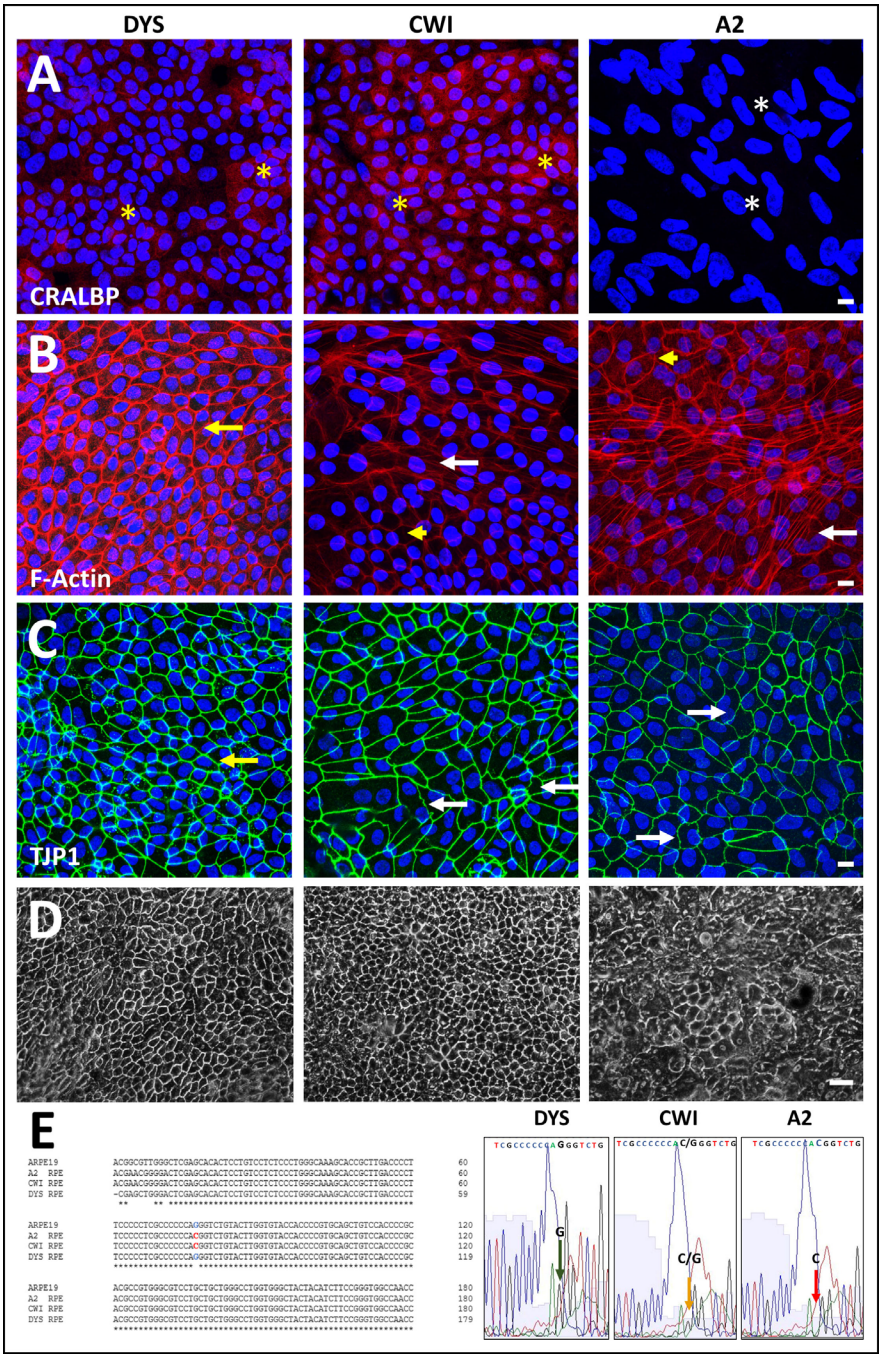

Figure 1. Comparison of control (DYS) and SLOS-derived (CWI, A2) iPSC-RPE cell morphology and genotype. Comparison of CRALBP and ZO1/TJP1 expression and F-actin organization in control (DYS) and SLOS-derived (CWI, A2) iPSC-RPE cells. Immunohistochemical (IHC) analysis of (**A**) CRALBP, (**B**) phalloidin cytochemical staining of F-actin, and (**C**) TJP1, and in DYS, CWI, and A2 RPE cells. DYS RPE cells formed a continuous monolayer consisting of polygonal cells with well-defined TJP1-positive cell borders and variable cytoplasmic CRALBP expression levels (yellow asterisks, **A**). CWI cells exhibited some irregularity in their cell borders and, like DYS cells, variable cytoplasmic CRALBP expression (yellow asterisks, **A**), while A2 RPE cells had low to absent CRALBP expression (white asterisks, **A**). DYS RPE cells exhibited predominantly lateral, cortical F-actin (yellow arrow, **B**). Increased F-actin stress fiber formation was evident in both SLOS-derived RPE cell lines, especially in A2 RPE cells (white arrows, **B**), however, both SLOS RPE also exhibited normal lateral, cortical F-actin labeling (yellow arrowheads, **B**). TJP1-positive cell borders appeared uniform in DYS RPE cells (yellow arrow, **C**), but irregular in some CWI RPE cells (white arrows, **C**). A2 RPE cells exhibited heterogeneity, with areas of regular cell border contacts, and areas of highly irregular and undulating TJP1 immunolabeling (white arrows, **C**). Scale bar (panels A-C): 10 µm. **D**: Lower-magnification phase contrast images of DYS, CWI, and A2 RPE cell cultures grown on poly-L-ornithine coated dishes for transcriptomic and protein expression analyses. Scale bar: 50 µm. **E**: Genotype and Sanger sequence verification of IVS8G-C mutation site confirming its heterozygous (CWI, yellow arrow, small G peak and merged C peak) and homozygous (A2, red arrow, G peak absent, merged C peak) state in SLOS-derived RPE cells, respectively. DYS RPE cells and ARPE-19 cells served as negative biological controls.

were washed with PBS and then fixed in PBS-buffered 4% paraformaldehyde. Free aldehydes were quenched by treatment with a solution of 100 mM glycine (pH 8.0) for 15 min at room temperature. Blocking and permeabilization were performed by incubating the cells in Tris-buffered saline with 0.1% (v/v) Tween (TBST), supplemented with 0.5% (w/v) BSA, 1% fish skin gelatin (w/v), and serum from appropriate host species corresponding to secondary antibodies (5%, v/v), for 45 min at room temperature. Primary antibodies were diluted as indicated above (Basal media and antibodies) in TBST containing 0.5% BSA, incubating overnight at 4 °C in a humidified chamber. Unbound antibodies were removed by three washes in TBST. We detected primary antibody binding by incubating the samples with appropriate dye-conjugated secondary antibodies (corresponding to host species of primary antibodies) at 1:500 dilution in TBST. Cell nuclei were counterstained with DAPI (4′,6-diamidino-2-phenylindole dihydrochloride). Rinzl coverslips were mounted onto glass microscope slides using Fluoro-Gel with PIPES buffer (1,798,540, EMS) face-side-up. Images were acquired with a scanning laser confocal fluorescence microscope (Leica TCS SPEII DMI4000, Leica Microsystems, Buffalo Grove, IL), applying the same laser settings for imaging DYS, A2, and CWI cells in each experiment, and using either a 40X or a 63X oil immersion (RI:1.518) objective.

Oil Red O staining of iPSC-RPE cells: All three RPE cell lines were cultured (n = 3/cell line) on Rinzl coverslips in high calcium-containing media for ~2.5 months. Detection of lipid droplets was performed by Oil Red O (MAK194, Millipore Sigma) staining, as per the manufacturer's protocol. Oil Red O working solution was prepared by adding 3 parts of Oil Red O solution to 2 parts of water, followed by filtration (after 20 min of incubation), using a 0.4 µm filter. RPE cells were fixed in 4% formaldehyde (buffered in PBS) for 10 min on ice. The fixative was washed with PBS three times, followed by treatment of coverslips with 60% isopropanol for 5 min. Cells were treated with freshly prepared Oil Red O working solution for 20 min at room temperature. Cells were washed with deionized water at least 3 times to remove any precipitate. Cells were incubated in Mayer's hematoxylin solution (MHS32, Millipore Sigma) for 1 min, followed by three washes in water. Cells were mounted and coverslipped, and light images were captured using an Olympus BH2 light/epifluorescence microscope.

IVS8G-C mutation analysis in SLOS iPSC-RPE cells: DHCR7 mutations in CWI and A2 iPSC-RPE cells were confirmed by PCR amplification of the appropriate genomic region (T93M mutation and intron-exon junction IVS8G-C), as described elsewhere [19]. Normal control iPSC-RPE (DYS) cells and ARPE-19 cells did not contain *DHCR7* mutations. Primers used to amplify the mutant region were as follows: Fwd 5′ – CAGAGGCAGAGCTGGGG – 3′ and Rev 5′- CAGCAGGCGGTAAGGCA – 3′ (yielding a 557 bp PCR product upon gel electrophoresis). Gel-excised PCR products (QIAquick® Gel Extraction Kit, Qiagen, cat. #28704) .were sequence verified (pay-for-service) at Roswell Park Cancer Institute (RPCI) Genomics Shared Resource (Buffalo, NY). Sequence readouts corresponding to the IVS8G-C region from ARPE-19 cells and DYS, CWI, and A2 iPSC-RPE cells were aligned and compared using the Clustal Omega Multiple Sequence Alignment program [26].

Steady-state sterol analysis: Sterol analysis of cultured iPSC-RPE cells was performed essentially as described in detail elsewhere [19,27]. In brief, cells were saponified, the non-saponifiable lipids were extracted with petroleum ether, the extract was dried under Argon gas and re-dissolved in MeOH, and analysis was performed using reverse-phase HPLC. The response factors and retention times for authentic standards of Chol and 7DHC were determined empirically. The following retention times were obtained: Chol, 16.65 ± 0.1 min; 7DHC, 15.1 ± 0.1 min. The integrated peak areas for Chol and 7DHC peaks were quantified using Flo-ONE™ software (Packard Instrument Co., Inc., Meriden, CT), and the 7DHC/Chol mole ratios were calculated; the data were subjected to statistical analysis using an unpaired Student's *t* test, with the cutoff for statistical significance set at $p < 0.05$ (n = 3/group).

RNA isolation, library preparation, and sequencing: Total RNA was extracted from individual iPSC-RPE samples using a RNeasy Plus Mini Kit (Qiagen; Germantown, MD), according to the manufacturer's instructions. RNA quantity and quality were determined using an RNA Nano 6000 kit (Agilent Scientific Instruments, Santa Clara, CA) on an Agilent BioAnalyzer 2100. RNA libraries were prepared from 100 ng of total RNA of each sample with a RIN >9.0 using a SureSelect Strand-Specific RNA Library Prep kit (Agilent), according to the manufacturer's protocol, and each sample was uniquely indexed for multiplexing. Library sample quantity and quality were determined using the DNA High Sensitivity kit (Agilent) on an Agilent Bioanalyzer 2100. Six samples were multiplexed and clustered at 8 pM in two lanes of a flow cell. We performed a 101 bp paired-end sequencing on an Illumina HiSeq 2500.

SDS-PAGE/Western blot analysis: Protein lysates from iPSC-RPE were prepared from triplicate monolayers cultured concurrent with those harvested for RNA isolation, using RIPA buffer (9806, CST, Danvers, MA), supplemented with protease inhibitors (P8340, Millipore Sigma). Samples were sonicated (4X for 3 s pulses, on ice), and clarified by

centrifugation at 15,000 × *g* for 15 min at 4 °C. The supernatants were assayed for total protein content using a Micro BCA™ Protein Assay Kit (23,235, Thermo Fisher Scientific), and equal amounts of total protein were subjected to SDS-PAGE (10% Bis-Tris NP0316, Thermo Fisher Scientific). Proteins were electrophoretically transferred to low-fluorescence PVDF membrane (1,620,264, Bio-Rad, Hercules, CA) for Western blot analysis as previously described [28] and probed with primary antibodies and alkaline phosphatase conjugated secondary antibodies (see the section *Basal media and antibodies*). Antibody binding was detected using a chemifluorescent enzyme substrate (45–000–947, Cytiva, Marlborough, MA) and imaged using a Chemidoc MP system (Bio-Rad). Densitometric analyses were performed using ImageLab® 5.0 software (Bio-Rad), and probed target band intensities were normalized to α-Tubulin levels. Data were subjected to statistical analysis using an unpaired Student's *t* test, with the cutoff for statistical significance set at $p < 0.05$ (n = 3/group).

RNA-seq data analysis: Reads were aligned to the human genome version hg38 analysis set, which does not include alternate contigs, using STAR (v2.5.2b). A non-redundant transcriptome database was derived from Gencode v24 and lincRNA annotation databases available on the UCSC Genome Browser [29] Raw counts for each exon were generated using RSubread (v1.24.1) and were summed over each isoform [30,31]. Only reads uniquely mapped to one genomic location were included in the counts. Uniquely mapped reads falling within overlapping isoforms were counted as belonging to both isoforms, unless a splice junction unique to one particular isoform of a gene had zero reads, in which case that isoform was considered not expressed and given a zero count. Splice junctions were quantified using the output provided by the STAR alignment. Differential expression analysis was performed using DESeq, assessing all pairwise comparisons, and transcripts having at least twofold expression change and an adjusted $p < 0.01$ were considered significantly differentially expressed. Differentially expressed gene sets were imported into Panther to determine pathways with overrepresented transcripts. Downstream analyses were performed using custom scripts in Perl and R.

RESULTS

Comparison of control and SLOS iPSC-RPE cell morphology and genotype: We evaluated morphological differences between control (DYS) and SLOS-derived (CWI, A2) iPSC-RPE cells by phase-contrast microscopy and IHC analysis of mature, confluent monolayer cell cultures. Figure 1 shows IHC images obtained using anti-cellular retinaldehyde-binding protein (CRALBP, Figure 1A), fluor-conjugated phalloidin (to label F-actin; Figure 1B), and anti-zona occludens protein (tight junction protein 1 (TJP1); Figure 1C). Mature DYS and CWI RPE cells exhibited cytoplasmic CRALBP immunolabeling, albeit with noted cell-to-cell variability in staining intensity (yellow asterisks, Figure 1A). By contrast, CRALBP expression was low to absent in mature A2 RPE cells (white asterisks, Figure 1A). The F-actin cytoskeleton distribution in DYS RPE cells appeared predominantly circumferential (yellow arrow, Figure 1B), with occasional sparse stress fibers. By comparison, CWI and A2 RPE cells exhibited increased actin stress fiber formation (white arrow, Figure 1B) while maintaining areas of normal circumferential F-actin distribution (yellow arrowheads, Figure 1B), consistent with observations by others regarding cultured iPSC-derived RPE cells [32]. A2 RPE cells were highly pleomorphic, exhibiting marked variability in cell shape and size, regular polygonal packing, areas with highly irregular cell arrangement and borders, and F-actin stress-fiber formation (white arrows, Figure 1B). At the tight junctions, DYS RPE cells exhibited intense cell border-specific TJP-1 immunolabeling (yellow arrows, Figure 1C). However, the TJP1-positive cell borders in some CWI RPE cells appeared irregular (white arrows, Figure 1C). A2 RPE cells formed continuous ZO-1 borders with both straight cell–cell contacts and areas exhibiting highly irregular and undulating TJP1 immunolabeling patterns (white arrows, Figure 1C). Bright-field images of parallel cultured monolayers used for transcriptomics and protein analyses are shown in Figure 1D. Both DYS and CWI RPE monolayers exhibited a polygonal cobblestone-like appearance typical of normal mature RPE cells, with pigmentation (melanin) and phase-bright cell borders. By contrast, A2 RPE cells exhibited more heterogeneity, exhibiting areas with a regular polygonal arrangement, and areas exhibiting highly irregular cellular packing, density, and shape (Figure 1D). Genotype and DNA sequence analyses (Figure 1E) verified that DYS RPE cells were negative for the IVS8G-C *DHCR7* mutation (large G peak, green arrow, Figure 1E), whereas CWI RPE cells were confirmed heterozygous for the IVS8G-C *DHCR7* mutation (small G peak, merged multi-C peak, yellow arrow, Figure 1E), and A2 RPE cells were homozygous for that mutation (G peak absent, merged multi-C peak, red arrow, Figure 1E). ARPE-19 cells served as biologic controls and were negative for the IVS8G-C *DHCR7* mutation.

Occludin is a member of the tetraspanin 4 superfamily (containing four transmembrane α-helices) of proteins, which binds to cytoplasmic ZO1/TJP1 domains at tight junctions and is a key regulator of paracellular permeability in epithelial cells, including RPE cells [33,34]. DYS RPE

cells exhibited co-labeling with anti-occludin antibody and fluor-conjugated phalloidin (the latter binds specifically to F-actin), with sharply defined cell borders and predominantly continuous anti-occludin labeling at the tight junctions (Appendix 1). CWI RPE cells exhibited some irregular cell borders, with areas of undulating occludin labeling, whereas A2 RPE cells exhibited areas of discontinuous or highly undulating occludin labeling (yellow asterisks, Appendix 1). As described above, both CWI and A2 (SLOS-derived) RPE cells exhibited prominent stress fiber formation (white arrows, Appendix 1).

We further characterized the regional epithelial-mesenchymal transition (EMT) of A2 RPE cell monolayers by performing co-immunolabeling against fibronectin, a key extracellular matrix (ECM) component and an EMT marker in vitro and in vivo [35,36], and against occludin. Although DYS RPE cell monolayers were mostly uniformly labeled along their cell borders for occludin (red arrows, Appendix 2) and circumferential F-actin (yellow arrows, Appendix 2), they generally lacked fibronectin expression. A2 RPE cell monolayers exhibited some fibronectin-negative patches that possessed occludin-positive cell borders (red arrow, Appendix 2) and occludin-negative patches with marked fibronectin upregulation (yellow asterisk, Appendix 2), as well as increased actin stress fiber formation (yellow arrows, Appendix 2), indicating regional EMT. We noted that A2 RPE cell monolayers exhibited modest improvement in polygonality and phase-bright appearance of cell borders when cultured on poly-L-ornithine-coated Rinzl coverslips compared to growth on poly-L-ornithine-coated tissue culture plastic. However, A2 RPE cells cultured on poly-L-ornithine-coated Rinzl coverslips still underwent EMT, which varied in severity, with areas of marked stress fiber formation and areas exhibiting both normal and irregular cell packing (*see* above, and Figure 1, Appendix 1 and Appendix 2).

Characterization of overall gene expression: We generated RNA-Seq libraries (n = 6 technical replicates each) from each of the concurrently cultured iPSC-RPE cell lines. The libraries were sequenced on a HiSeq 2500, generating between 70 and 120 million raw reads. Two of the DYS samples failed to cluster before sequencing and were removed from further analysis. Gene expression was first characterized for the whole transcriptome to determine the quality of the sample preparations. Using STAR to align reads to the hg38 human genome build, over 80% of the reads from each sample were aligned. We used the GENCODE v24 annotation database to generate counts for both genes and isoforms [37]. We determined the specific isoforms expressed in the samples using the methods described previously [31]. Of the 65,439 genes and 113,246 isoforms in the annotation database, we detected 14,255, 14,891, and 13,521 genes and 31,976, 33,291, and 28,688 isoforms (RPKM >1) in the A2, CWI, and DYS iPSC-RPE samples, respectively (Figure 2A). Intra-sample concordance was high among the samples (range: 0.96–0.99). Inter-sample concordance, however, was relatively high between A2 and DYS (0.90) RPE cells but was lower when we compared CWI to DYS (0.78) and A2 to CWI (0.65) RPE cells. In concordance with the negative binomial distribution of the RNA-Seq data, most transcripts had an RPKM <1, which we considered to indicate no expression (Figure 2A). This is in agreement with a principal component analysis showing that the replicate samples were clustered together, although each condition was separate (Appendix 3).

We then compared the overlap of isoform expression. Among the three sample types, 25,589 isoforms were expressed in all, which corresponds to 77%–89% of the total isoform expression. However, the two SLOS patient-derived samples showed the highest degree of overlap (29,165). In contrast to the inter-sample concordance, CWI and DYS RPE cells showed a higher degree of overlap in isoform expression (27,317 isoforms) than A2 and DYS RPE cells (26,027 isoforms; Figure 2B).

We also considered the RPKM distribution of isoform expression as a function of relative transcript levels. We counted the number of transcripts across 6 RPKM bins: 0–1 (*not expressed*), 1–10, 10–100, 100–1000, and greater than 1000. Aside from the 100–1000 RPKM bin, in which CWI RPE cells showed more transcripts than average, the data across the remaining bins were consistent among the sample types (Figure 2A).

To examine the global expression differences between the conditions, we performed differential expression analysis using DESeq. We chose DESeq over DESeq2 to minimize the number of observed false positives [38]. We considered a transcript to be differentially expressed if it showed a fold change greater than 2 and an adjusted p <0.01, and we found significant differences in expression between all conditions. We saw the largest number of changes between A2 and DYS RPE cells, where we found 20,091 transcripts either significantly upregulated or downregulated (Figure 2C). Of these, the largest number (8,654 transcripts) fell into the 2- to 5-fold change group. Interestingly, the second largest number (4,251 transcripts) was either turned on or off in the A2 iPSC-RPE cell line. Comparing CWI and DYS RPE cells, we found 14,192 differentially expressed transcripts (Figure 2C). Again, most of these transcripts fell into the 2- to 5-fold change (7,348 transcripts) and the on/off group (3,403

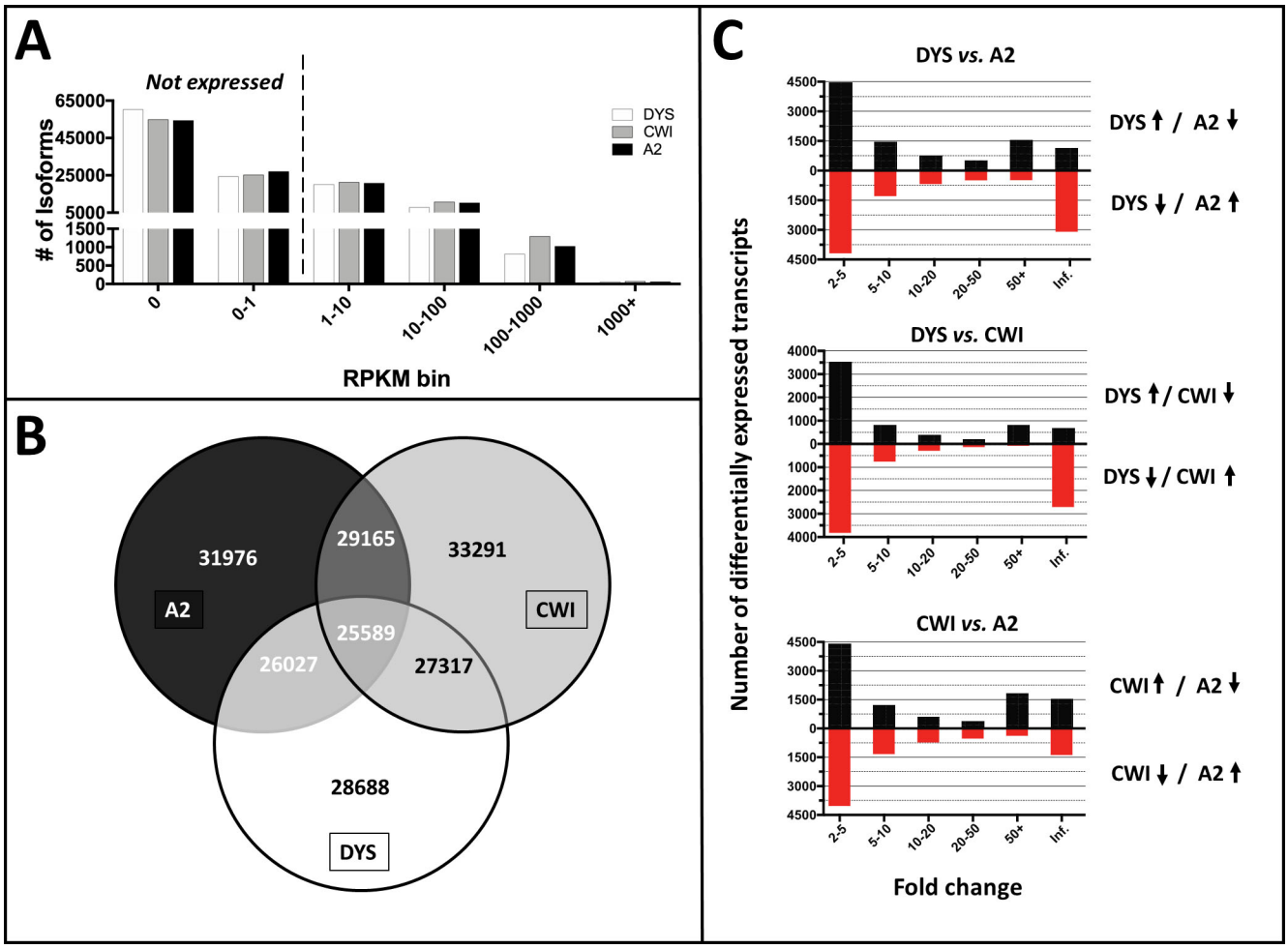

Figure 2. Whole transcriptome analysis of SLOS-derived (CWI and A2) versus control (DYS) iPSC-RPE cells. **A**: Of the 65,439 genes and 113,246 isoforms in the GENCODE24 annotation database, expression of ~14,500 genes was detected in all three cell lines (see color key, *inset*), with 31,976, 33,291, and 28,688 isoforms detected (RPKM >1) in the A2, CWI, and DYS RPE samples, respectively. RPKM values of <1 are considered as non-expressed isoforms/transcripts. **B**: All three RPE cell lines had 25,589 isoforms in common, which corresponds to 77%–89% of the total isoform expression. However, the two SLOS-derived (CWI and A2) samples showed the highest degree of overlap (29,165 isoforms). In contrast to the inter-sample concordance, CWI and DYS RPE cells showed a higher degree of overlap in isoform expression (27,317 isoforms) than did A2 and DYS RPE cells (26,027 isoforms). **C**: Bar graph representation comparing upregulated and downregulated isoforms in DYS versus A2, DYS versus CWI, and CWI versus A2 RPE cells, respectively, as a function of fold change.

transcripts). We also found many transcripts significantly different between the two SLOS phenotypes ("mild" versus "severe"), with 18,430 differentially expressed transcripts between the A2 and CWI RPE cells, 8,439 with a 2- to 5-fold change, and 2,933 in the on/off category (Figure 2C).

Protein and transcriptome characterization of RPE and EMT biomarker expression: We analyzed the protein and transcriptome expression profiles of key RPE and EMT markers. Protein lysates were prepared from mature (2.5 months in culture) control and SLOS-derived RPE cell monolayer cultures (n = 3 per iPSC RPE cell line). Parallel monolayers were used for Western blot and RNA-Seq analyses (see Methods, Figure 3B). Transcriptomic analysis revealed that several known EMT marker transcripts were expressed at significantly higher levels in CWI SLOS and A2 SLOS RPE compared to DYS, and that a subset was upregulated in A2 with respect to CWI (Appendix 4). Protein-level expression of RPE markers (CRALBP, BEST1, and RPE65) was observed in all three iPSC-RPE cell lines by Western blotting, albeit at different levels (Figure 3A,B). The two SLOS-derived iPSC-RPE lines exhibited significantly higher β-actin (ACTB) levels compared to DYS iPSC-RPE cells, despite uniform protein content loading (Figure 3A). Therefore, α-tubulin (TUBA1A) content was used as the "housekeeping" protein for normalization, due to its lower variance among the three

cell lines than ACTB (Figure 3A, B). The visual cycle protein CRALBP was expressed at similar levels in CWI and DYS iPSC-RPE cells, but A2 iPSC-RPE cells exhibited significantly lower levels (~0.08-fold, normalized to TUBA1A, relative to DYS, p <0.01, n = 3; Figure 3B). The cytoskeletal linker Ezrin was expressed robustly in both DYS and CWI cells, albeit at slightly lower levels in CWI after normalization, whereas A2 SLOS expressed ~5-fold lower levels of Ezrin compared to DYS cells, indicating less epithelial differentiation and polarization (p <0.01, n = 3; Figure 3B). Expression of RPE65 and E-cadherin were significantly higher in CWI iPSC-RPE cells compared to DYS RPE cells (~4-fold and ~5-fold, respectively, p <0.01, n = 3, Figure 3B), whereas A2 iPSC-RPE cells exhibited the lowest expression levels of these differentiation markers (~0.5- fold and ~0.1-fold, respectively, relative to DYS, p <0.01, n = 3; Figure 3B). Bestrophin-1 (BEST1), a calcium-signaling regulator, was expressed in all three iPSC-RPE cell lines at basal levels, with lower levels in both SLOS iPSC-RPE lines versus DYS iPSC-RPE cells (p <0.05; Figure 3B). Vimentin, a known EMT marker in vivo [39], was robustly expressed in all three mature iPSC RPE lines (Figure 3A,B). However, it is well established that vimentin is expressed in immortalized bovine and other RPE culture models in vitro [40,41]. Interestingly, we observed a typical degradation pattern for vimentin, producing a species smaller by ~8–10 kDa than full-length ~58 kDa vimentin, consistent with its processing by either calpain or caspase family proteases [42,43]. A2 SLOS RPE expressed modestly higher levels of vimentin protein compared to CWI and DYS RPE, in agreement with the transcript levels of vimentin across the three cell lines (Appendix 4). We then compared the levels of α-smooth muscle actin (SMA), an established EMT marker. Compared to DYS iPSC-RPE cells, we observed significantly elevated levels of SMA in both A2 (~20-fold, p <0.01, n = 3) and CWI (~3.7-fold, p <0.01, n = 3) iPSC-RPE cells (Figure 3B). Transcriptomic analysis showed significant increases in the expression levels of several EMT markers (*SNAI1, SNAI2 (SLUG), TWIST1, ZEB1, CDH2 (N-Cad), CDH1 (E-Cad), VIM, HMGA2)* in A2 and CWI SLOS RPE cells versus DYS iPSC-RPE cells (Appendix 4).

We employed the RPE signature gene set developed by other [44], which consists of 86 genes and 292 isoforms [31]. We found that both CWI and DYS iPSC-RPE cells expressed 85 genes, consistent with our previous findings, whereas A2 iPSC-RPE cells expressed 82 of the 86 RPE signature genes. This corresponds to 225, 245, and 224 isoforms of RPE signature genes for DYS, CWI, and A2 RPE cell lines, respectively. A comparison across the three sample types of the relative expression levels of the RPE signature genes showed that A2 RPE cells had more low-expressing genes, whereas CWI and DYS RPE cells had more medium-to-high-expressing genes (Figure 3C). We compared the distribution of RPE signature gene expression levels across all three RPE cell lines and found that A2 cells had more transcripts with RPKM <10, but CWI and DYS cells had more transcripts with RPKM greater than 100 (Appendix 5A). This pattern was confirmed by the observed concordances. A Pearson correlation of CWI and DYS cells showed that the samples were tightly correlated (0.92), but very low concordance was observed between either CWI (0.05) or DYS (0.13) and A2 iPSC-RPE cell lines (Appendix 5B). In general, although the A2 cells expressed genes consistent with being RPE cells, their expression levels were dissimilar to those of both CWI and DYS cells.

Although gene expression data suggested that the A2 and CWI iPSC-RPE cells were distinguishable from DYS iPSC-RPE cells, pathway analysis revealed several common upregulated biologic process pathways in common between the two. DYS iPSC-RPE cells were also highly pigmented (melanized), consistent with *RAB38* (ras-related protein Rab38) and *TYRP1* (tyrosine-related protein 1) expression, as seen in transcriptome analysis (Figure 3C,D (inset)). By comparison, both SLOS-derived RPE cell lines, especially CWI cells (with lower *TYRP1* expression, Figure 3C), exhibited reduced melanin content compared to DYS cells (Figure 3D, (*inset*)). Comparisons of A2 and CWI RPE cell data to the DYS line showed that eight of the top 20 most significant pathways are shared between the two disease lines (Figure 3D). These include features known to be important to RPE cells, including cell junction assembly, cell-substrate adhesion, extracellular matrix organization, and response to oxidative stress. Interestingly, the individual comparison of A2 versus DYS iPSC-RPE cells revealed that four actin pathways were significantly overrepresented in the former, which corresponds to the actin findings in the phenotype experiments (Figure 3D).

Sterol quantification of RPE cell lines: We tested the effects of *DHCR7* mutations on sterol biosynthesis in the three RPE cell lines. Mature RPE cells (2.5-month cultures) were maintained in a sterol-replete medium containing 0.9% (v/v) bovine calf serum (BCS). Under this culture condition, RPE sterol homeostasis is driven by a combination of cellular de novo sterol synthesis and endocytic uptake of Chol-laden LDL particles [45]. Reverse-phase HPLC analysis of non-saponifiable lipid extracts from DYS, CWI, and A2 iPSC-RPE cells revealed that A2 cells cultured in sterol-replete medium exhibited significantly elevated 7DHC/Chol mole ratios (0.63 ± 0.08, avg. ± SEM, p <0.01, n = 3), as compared

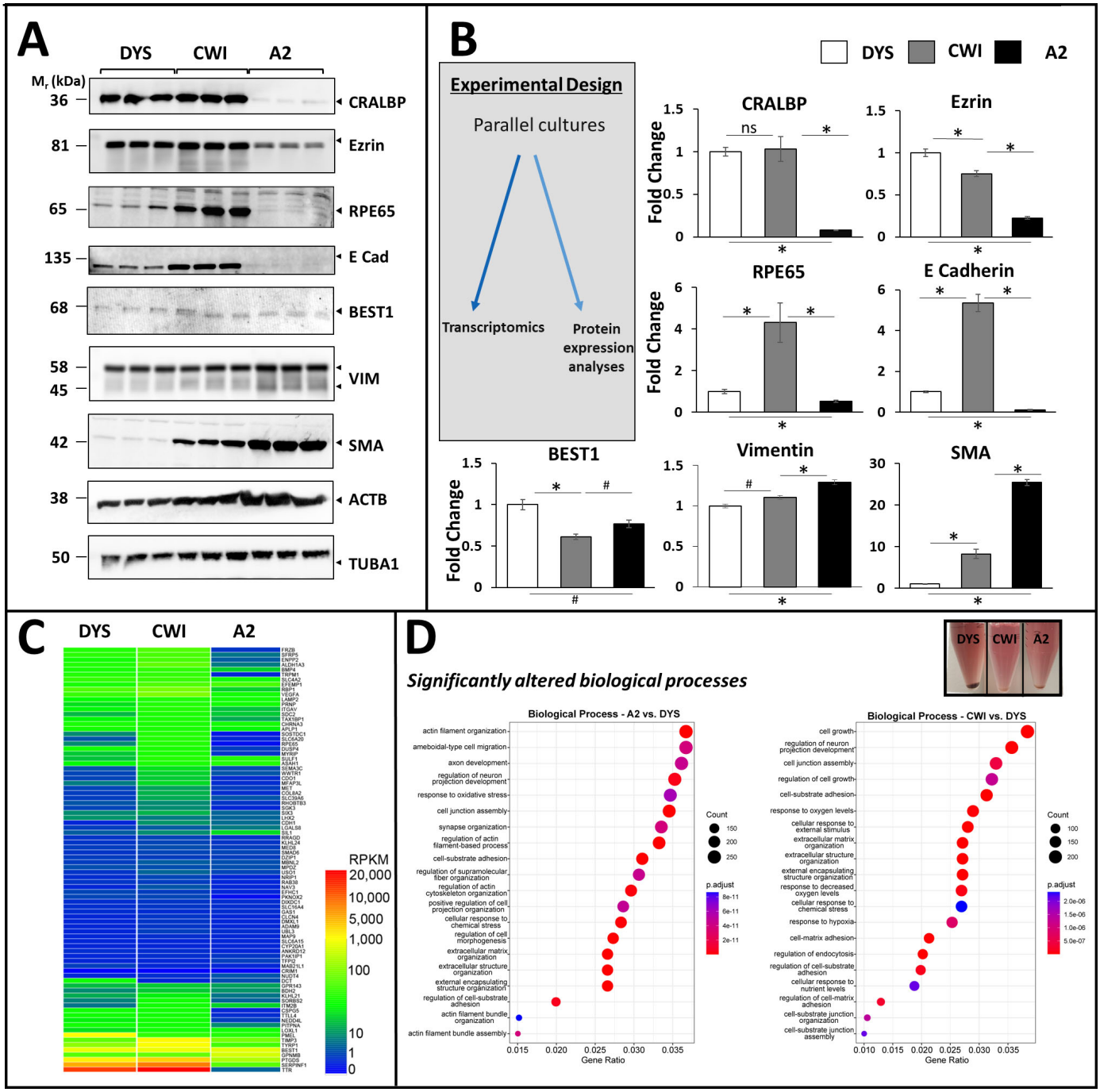

Figure 3. Characterization of RPE and EMT protein biomarker expression in control (DYS) and SLOS-derived (CWI, A2) iPSC-RPE cells. **A**: Western blot analysis of CRALBP, BEST1, RPE65, cytoskeletal and EMT marker expression in all three RPE cell lines. A2 RPE cells exhibited markedly lower levels of visual cycle proteins RPE65 and CRALBP, and lower levels of cell adhesion and cytoskeletal linkers E-cadherin and ezrin, compared to CWI and DYS RPE cells. Best1 was expressed in all three RPE lines albeit at slightly varying levels. CWI and A2 RPE cells expressed higher levels of α-smooth muscle actin (SMA), an EMT marker, compared to DYS RPE cells. Vimentin was expressed in all three RPE cell lines and appeared variably cleaved to ~45 kDa, with modest elevation in A2 cells. α-Tubulin (TUBA1) expression was found to be a more reliable (less-variable) "house-keeping" gene product, as compared to β-actin (ACTB); hence, TUBA1 was employed for normalization of expression levels (see panel **B**). **B**: Fold-change values (based on semi-quantitative densitometry) for RPE and EMT protein markers in SLOS-derived vs. control RPE cells, normalized to TUBA1 (n=3, *p<0.01, # p<0.05). **C**: Heatmap of RPKM levels for the RPE signature genes identified by Liao et al. (30) in each of the iPSC-RPE cell lines. Between 82 (A2) and 85 (CWI and DYS) of the 86 signature genes were expressed in the iPSC-RPE cell lines, albeit many at low levels. **D**: Dot plot representation of Pathway analysis of Biological Processes using clusterProfiler. Cell junction assembly, cell-substrate adhesion, extracellular matrix organization, and actin cytoskeleton-associated pathways were found to be significantly altered in both of the SLOS-derived RPE cell lines, vs. DYS RPE cells. (**Inset**): Image of cell pellets derived from the three RPE cell lines, demonstrating that the melanin content of DYS RPE cells was substantially greater than that of CWI and A2 RPE cells.

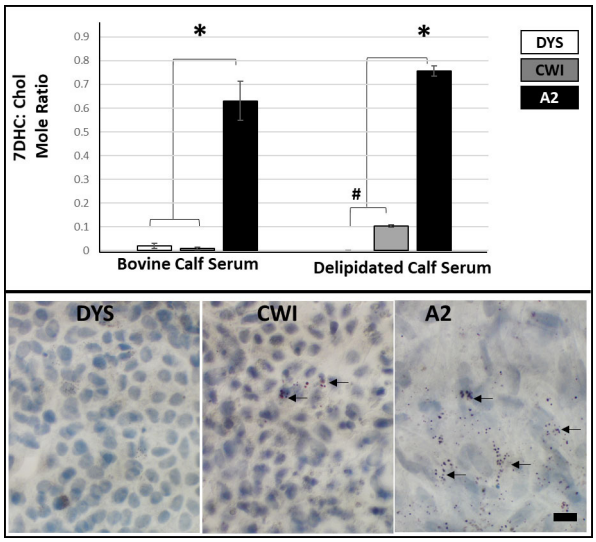

Figure 4. Effect of presence or absence of exogenous Chol in the culture medium of DYS, CWI, and A2 RPE cells on cellular sterol profiles. 7DHC/Chol mole ratios were quantified by reverse-phase HPLC analysis of non-saponifiable lipids extracted from cells cultured for 9 days in medium containing either 0.9% (v/v) bovine calf serum (BCS) or delipidated (sterol-deficient) calf serum (DLCS). **Upper panels**: 7DHC/Chol mole ratios (average values, n = 3/each condition/cell line) are expressed as a function of the culture condition. A2 RPE cells exhibited the highest levels of 7DHC, enhanced by culturing in the DLCS-containing medium. When cultured in medium containing BCS, the sterol profile of CWI RPE cells was comparable to that of DYS (control) RPE cells; however, 7DHC levels increased significantly when CWI RPE cells were switched to DLCS-containing medium, whereas the DYS RPE cells did not respond similarly (n = 3, *p <0.01, #p <0.05). **Lower panels**: Light microscopy images of Oil Red O-stained SLOS-derived (CWI and A2) RPE cells and control (DYS) RPE cells (n = 3/ cell line). A2 RPE cells exhibited substantial accumulation of lipid droplets, while only select CWI RPE cells exhibited lipid droplet accumulation *(*black arrows). By contrast, DYS RPE cells did not exhibit lipid droplet accumulation. Scale bar: 10 µm.

to DYS and CWI iPSC-RPE cells, which contain negligible amounts of 7DHC (Figure 4, top panel). Surprisingly, CWI iPSC-RPE cells exhibited a normal sterol profile (comparable to that of DYS cells) when cultured in BCS-containing medium (Figure 4, top panel), despite harboring verified compound heterozygous *DHCR7* mutations (Figure 1E). However, when mature A2 and CWI iPSC-RPE cells (initially cultured in medium containing 0.9% BCS for 2 months) were switched to medium containing 0.9% delipidated calf serum (DLCS without serum lipoproteins/Chol) for 9 days, they both exhibited increased levels of 7DHC formation and accumulation, as demonstrated by elevated 7DHC/Chol mole ratios (0.75 ± 0.02 and 0.1 ± 0.005, respectively), compared to DYS RPE cells maintained in delipidated medium (Figure 4, top panel). However, A2 iPSC-RPE cells consistently exhibited significantly higher 7DHC content than CWI iPSC-RPE cells under both experimental conditions (Figure 4, top panel). This observation is consistent with our prior report of 7DHC accumulation in CWI iPSC-RPE cells cultured in a medium containing 0.9% DLCS, suggesting that these cells possess an active Chol homeostasis process modulated by the presence or absence of exogenous (serum-borne) lipoproteins in the medium [19,46].

Previous studies have shown significant lipid and sterol accumulation in SLOS patient fibroblasts [47]. We independently observed lipid droplet accumulation in the RPE of the AY9944 rat model of SLOS [18]. We used Oil Red O staining to test for lipid droplet accumulation in both SLOS-derived and control cultured iPSC-RPE cells (mature cultures maintained in 0.9% BCS-containing medium for 2.5 months on Rinzl coverslips; n = 3/cell line). We consistently observed substantially greater lipid droplet accumulation in A2 RPE cells than in CWI RPE cells; very few of the latter exhibited lipid droplets (black arrows, Figure 4, bottom panel). By contrast, DYS RPE cells appeared healthy and did not show lipid storage abnormalities (Figure 4, bottom panel).

DISCUSSION

In this study, we integrated data from three RNA-Seq libraries prepared from individual iPSC-RPE cell lines (derived from reprogrammed fibroblasts) from one normal patient (DYS), one mildly affected (CWI) SLOS patient, and one severely affected (A2) SLOS patient. We observed extensive remodeling of F-actin, and markedly elevated stress fiber formation in both SLOS-derived (CWI and A2) RPE cell lines when compared to control (DYS) RPE cells. This was accompanied by significant increases in SMA levels in both CWI and A2 RPE cell lines compared to DYS RPE cells, indicative of reversion to a more migratory and mesenchymal phenotype. We also noted that changes to the ECM occurred in A2 cells undergoing EMT, with observed changes in fibronectin expression levels in regions where cell borders and cell–cell

contacts are compromised. Importantly, we observed marked monolayer heterogeneity in cultured A2 RPE cells: whereas some areas of the monolayer appeared phase-bright and polygonal, intervening regions appeared more fibrotic-like and clearly exhibited loss of cell–cell contact; moreover, fibronectin was expressed in A2 RPE cells undergoing EMT.

Pathway analysis of A2 versus DYS iPSC-RPE cells revealed the overrepresentation of four actin pathways in SLOS-derived RPE cell lines, along with alterations in cell junction assembly, cell-substrate adhesion, and ECM organization. These findings are fully consistent with the irregular appearance of TJP1-positive cell borders in some CWI RPE cells (i.e., minor to moderate disorganization of the TJP1 immunolabeling pattern in a subset of CWI cells) and in areas of the A2 RPE cell monolayers that were undergoing EMT, including some regional loss or discontinuity of occludin immunolabeling, in comparison to the more uniform and stably differentiated DYS RPE cells. Such alterations in cell border and monolayer organization are observed in SLOS-derived RPE cell lines despite the expression of >90% of RPE markers in all three RPE cell lines. The transcript levels of RPE markers (and their isoforms) in A2 RPE cells were significantly lower than those in CWI and DYS RPE cells. We also observed significantly decreased levels of CRALBP protein in both CWI and A2 RPE cell lines relative to the control (DYS) RPE cells. Interestingly, RPE65 levels were higher in CWI cells than in DYS and A2 RPE cells. RNA-Seq data further showed a decrease in highly expressed transcripts in A2 RPE cells compared to the other two RPE cell lines employed in this study. This may be due to the general downregulation of transcriptional machinery in A2 RPE as a response to increased oxidative stress in SLOS, as shown by us recently [48]. Based on the pathway analysis, “response to oxidative stress” was identified as a highly significant pathway that is dysregulated in A2 RPE **(**Figure 3), which may be a result of the increased levels of 7DHC (a highly oxygen-labile organic compound) observed in the sterol quantification studies. Indeed, marker expression may vary between biologic and clonal sources of iPSC-RPE cells, as well as being subject to culture conditions.

Further, our transcriptomic analysis showed a significant increase in well-established markers of EMT [49-51] in SLOS RPE cell lines compared to control RPE cells. The above results indicate a degree of variability in cellular responses and differentiation status, even within the same clonal population of cells. However, neither EMT nor patient genetic background can account for the significant accumulation of 7DHC in SLOS-derived iPSC-RPE cells; this feature is solely due to sequence-verified ‘mild’ and ‘severe’ *DHCR7* mutations. It has been established that accumulation of the Chol precursor 7DHC leads to the formation of 7DHC-derived oxysterols [52], and accumulation of such oxysterol species can cause cellular transcriptional changes in other iPSC or cell culture models [20,23,52,53]. Previous independent investigations of whole-genome cDNA transcripts from iPSCs obtained from severely affected (A2) SLOS patients versus control patients have demonstrated that EMT transcriptional network upregulation occurs in A2 iPSCs, specifically under conditions of Chol depletion [20], and we have observed this same phenomenon in RPE cells derived from those same iPSCs. However, lipoprotein supplementation in the media reversed the occurrence of EMT [20]. We recognize that differences in donor genetic background may, to some extent, contribute to the observed phenotype–transcriptome correlates in our control and disease iPSC-derived RPE models. In vitro *DHCR7* gene correction in CWI and A2 RPE cells may serve as ideal congenic controls to fully negate the effects of donor genetic background. However, such experiments are beyond the scope of the current study.

We verified the biochemical sequelae of the onboard *DHCR7* mutations in CWI and A2 RPE cells (versus control DYS RPE cells) by measuring the 7DHC/Chol mole ratio under culture conditions, with or without exogenous Chol (0.9% BCS and 0.9% DLCS, respectively). This is because cellular Chol homeostasis is dependent on both endocytic sterol uptake and de novo synthesis [45]. We found that CWI RPE cells (compound heterozygous, harboring both the hypomorphic T93M and the splice acceptor IVS8-1G>C *DHCR7* mutations) cultured under sterol-replete conditions had the capacity to maintain essentially a normal sterol profile by sterol uptake from the culture medium (Figure 3). However, CWI RPE cells cultured under sterol-deficient conditions (0.9% DLCS for 9 days) exhibited significantly elevated cellular 7DHC content, consistent with our previous observation [19]. A similar trend was observed with A2 RPE cells as well; however, owing to the homozygous DHCR7 mutation in A2 RPE cells (associated with a “severe” SLOS phenotype), we observed significant 7DHC accumulation under *both* sterol-replete and sterol-deficient culture conditions. The observed increase in 7DHC/Chol mole ratio upon culturing in delipidated serum-supplemented media (for 9 days) strongly suggests de novo sterol synthesis ability in RPE cells. However, this observation does not faithfully reflect sterol synthetic rates due to the observed lipid droplet accumulation in CWI and A2 SLOS RPE cells, which may possibly lead to sterol accumulation and efflux defects [45,47]. These observations suggest that these iPSC-RPE cells have the capacity for compensatory uptake of exogenous lipoproteins.

When comparing the two SLOS patient-derived, iPSC-RPE cell lines in this study, the added intersection of SLOS disease phenotypes (of which there are many, ranging from mild to severe, with no obvious genotype–phenotype relationship [3]) further complicates the characterization of disease-driven changes in cell physiology and morphology, in turn confounding the delineation of those effects from de-programming, senescence, and EMT iPSC-functionalities. We therefore approached the characterization of each cell line using multiple methods of analysis, including assessing F-actin cytoskeletal features and distribution, RPE and EMT protein marker expression profiles, sterol composition (7DHC/Chol mole ratio), cellular monolayer morphological characteristics, and de-differentiation (as for A2 RPE cells) over a period of 2–2.5 months in culture. The overall findings of the study are represented schematically in Figure 5.

Pharmacological rodent models of SLOS have previously implicated the RPE as a contributor to the progressive irreversible retinopathy observed in these models [18,19]. However, in vivo investigation of RPE-specific sterol profiles and transcriptome changes is challenging. In the current study, we sought to circumvent these limitations by thorough morphological, molecular, and transcriptome analyses of SLOS patient-derived, iPSC-derived RPE cells using iPSC-RPE cells derived from a normal, approximately age-matched human subject. We found that the accumulation of 7DHC in SLOS-derived iPSC-RPE cells correlated with altered RPE morphology (cell shape, tight junction formation), decreased RPE protein marker expression, and EMT. The findings of this study may suggest that RPE-specific inhibition of DHCR7 activity may be sufficient to trigger the RPE pathology observed in vivo. Future investigations using the SLOS-derived iPSC-RPE cells described herein will involve in vitro gene supplementation and the generation of iPSC-RPE cells from *Dhcr7* null fibroblasts and simple pharmacological approaches to rescue the observed RPE defects. Further, we aim to characterize RPE pathology in vivo by targeted depletion of *Dhcr7* in mouse RPE cells. Using these approaches, we will be able to differentiate between *disease*-driven versus iPSC-driven processes and evaluate the specific effects of the *Dhcr7* and Cho pathways on RPE phenotypes.

Limitations of the present study: To characterize individual iPSC-RPE lines and assess differentiation, several limitations need to be considered. A limitation of the use of reprogrammed iPSC-derived RPE cell models is the low passage numbers compared to immortalized, transformed cell lines such as ARPE-19 [54–56]. Differentiated iPSC-derived RPE cells in culture may lose their epithelial-like characteristics and exhibit loss of specialized cell–cell contacts [57], reversion to a fibroblastic-like phenotype, and acquisition of mesenchymal expression profiles and migratory properties; that is, they may undergo EMT [58,59]. The reorganization of F-actin and stress fiber formation are also additional indicators of EMT [60]. We identified the challenges in delineating

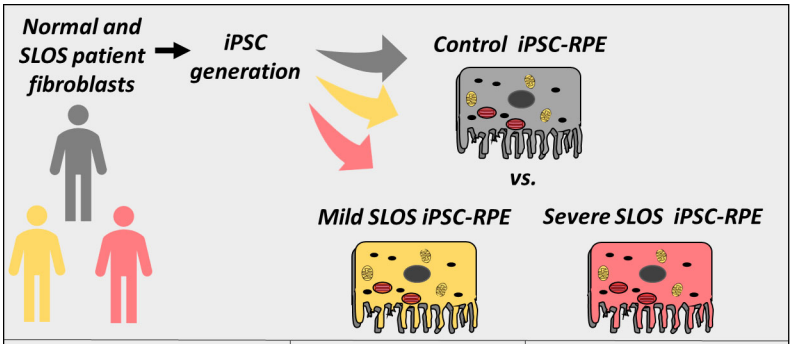

DHCR7 mutation	*T93M/IVS8-1G->C*	*IVS8-1G->C/IVS8-1G->C*
RPE markers	↓	↓↓↓
Epithelial-mesenchymal transition	*Mild in patches*	*Severe in patches*
Irregular tight junctions and stress fiber	↑	↑↑↑
7DHC accumulation	↑ *in delipidated serum*	↑↑↑ *in all conditions*
Lipid droplet accumulation	↑	↑↑↑

Figure 5. Schematic representation of the findings of the current study. Compared to normal human iPSC-derived RPE (DYS), SLOS iPSC-derived RPE cell lines (CWI and A2, respectively) exhibit moderate to marked decreases in RPE biomarkers, increase in EMT markers, and moderate to marked accumulation of 7DHC and lipid droplets.

iPSC-associated versus SLOS mutation-associated dedifferentiation/EMT that might have occurred in our cultured cell lines. However, comprehensive iPSC-based modeling of rare disorders, such as SLOS, is challenging. The generation of multiple iPSC-RPE lines per donor, along with appropriate isogenic controls, is time/labor/resource-intensive. The appearance of "normal" phase-bright regions among dedifferentiated areas of the same monolayers (that is, as seen in CWI and A2 SLOS-derived RPE cells) also suggests heterogeneity in the cultures, and that there may be more than one set of drivers for EMT. The observed elevation in the expression level of SMA, an EMT marker, in A2 and CWI RPE cells could be driven partly by the decreased functionality of DHCR7 in those cells. Indeed, the level of RPE marker expression observed in differentiated iPSC-RPE cells from multiple biologic and clonal sources is likely to vary from culture to culture, and we acknowledge that varied levels of EMT may arise under different culture conditions, for example, when using different basement membrane adhesion substrates or other growth conditions. These limitations of iPSC-derived RPE cells have been discussed elsewhere [61]. However, when iPSC-RPE cells were seeded and cultured under identical conditions, with identical (replicate) cultures used for both biochemical and transcriptome analyses, we were able to discern distinct control versus SLOS-dependent cellular phenotypes within the limits of the in vitro system used. The degree to which the observed EMT of A2 iPSC-RPE cells is *disease*-driven versus iPSC-driven is a complex issue. However, we have repeatedly observed that A2 iPSC-RPE cells are prone to undergoing EMT; hence, this appears to be a *bona fide* feature of the A2 phenotype.

APPENDIX 1.

To access the data, click or select the words "Appendix 1." Immunohistochemical analysis of occludin (*green*; anti-occludin, mAb OC3-F10) and cytochemical analysis of F-Actin (*red*; Alexa Fluor 568- conjugated phalloidin) of DYS, CWI, and A2 RPE cells. DYS RPE cells formed continuous monolayers constituted by polygonal cells with sharp occludin-positive cell borders. The F-actin cytoskeleton of DYS RPE cells appeared mostly lateral and cortical. In CWI RPE cells, occludin-positive cell borders often appeared irregular (*yellow asterisks*), with intermittent phalloidin-labeled F-actin stress fibers (*white arrows*). A2 RPE cells were highly heterogeneous, consisting of some occludin-negative, or discontinuous monolayer regions with aberrant, pleomorphic cell shapes, as well as regions of regularly arranged polygonal cells with occludin-positive cell contacts (*yellow asterisks*). A2 RPE monolayers exhibited varied F-actin stress fiber formation (*white arrows*). Scale bar: 20 µm.

APPENDIX 2.

To access the data, click or select the words "Appendix 2." Comparative immunohistochemical analysis of expression and distribution of fibronectin (an EMT marker) and occludin in control (DYS) and A2 SLOS iPSC-derived RPE cells. Occludin (*green*), fibronectin (*red*), and F-actin (Alexa Fluor 568-conjugated phalloidin, pseudocolored *gray*) in DYS (*upper panels*) and A2 (*lower panels*) RPE cells. DYS RPE cells formed a continuous, relatively uniform polygonal monolayer with predominantly occludin-positive tight junctions at the cell borders (*red arrows*), with no obvious fibronectin expression, and a circumferential pattern of F-actin (*yellow arrows*). By contrast, A2 RPE cells formed a heterogeneous monolayer, with regional occludin immunolabeling of tight junctions along polygonal cell borders (*red arrow*), but also some regions devoid of occludin at the tight junctions (*yellow asterisk*). Elevated fibronectin expression in regions exhibiting poor occludin immunolabeling of the cell borders was observed in A2 RPE cells (*yellow asterisk*). Regional F-actin stress fiber formation was evident in A2 RPE cell monolayers, especially in areas undergoing EMT (*yellow arrows*). Scale bar (all panels): 20 µm.

APPENDIX 3.

To access the data, click or select the words "Appendix 3." Principal Component Analysis using the RNA-Seq data from the A2 (*blue*), CWI (*green*), and DYS (*red*) iPSC-RPE cells. Each replicate clusters within its sample type. These data demonstrate low replicate-to-replicate variability and distinct differences between the sample types, *i.e.*, disease severity class ("mild" *versus*. "severe" SLOS) *versus*. normal control.

APPENDIX 4.

To access the data, click or select the words "Appendix 4." Analysis of EMT-associated genes in RNA-Seq data. **A.** DESeq normalized counts for known EMT-associated genes in DYS, CW1, and A2 iPSC-RPE. All of the EMT-associated genes, excluding *ZEB1*, are expressed to some degree in all three sample types. **B.** Nearly all of the EMT-associated genes are upregulated in the SLOS-derived (CWI and A2) are significantly upregulated relative to the DYS control line. The exceptions are *SNAI1, SNAI2,* and *ZEB1* in the CWI:DYS comparison. Additionally, all, but one (*CDH1*), are significantly upregulated in the more severe SLOS sample (A2) compared to the CWI sample, which has a milder phenotype.

INF=expression is observed in only one sample of the comparison.

APPENDIX 5.

To access the data, click or select the words "Appendix 5." **A.** Bar graph representation of RPE-specific gene isoforms expressed in all three iPSC-RPE cell lines (see color key), as a function of RPKM. SLOS-derived ("severe") A2 RPE cells exhibited lower levels of expression of RPE-specific gene isoforms than CWI ("mild," SLOS-derived) or DYS (control) RPE cells, especially in RPKM values greater than 100. **B.** Concordance analysis (through Pearson correlation) of RPE-specific gene isoforms showing high concordance between CWI and DYS RPE cells, but low concordance between A2 and DYS RPE cells or between A2 and CWI RPE cells.

ACKNOWLEDGMENTS

We gratefully acknowledge computational support provided by the Center for Computational Research at the University at Buffalo. Next Generation Sequencing services were provided by the Genomics Core at the Children's Hospital Los Angeles. We thank Kevin Francis (formerly at NICHD/NIH, currently at Sanford Research) and Forbes D. Porter (NICHD/NIH) for the human SLOS-derived iPSCs and Sally Temple (Neural Stem Cell Institute) and Barbara Corneo (Columbia University Stem Cell Core Facility) for converting the iPSCs to RPE cells. We thank Bruce A. Pfeffer for helpful discussions and suggestions throughout the course of this study. A preliminary report of portions of this work was presented at the 2018 Annual Meeting of the Association for Research in Vision and Ophthalmology (ARVO). The opinions expressed herein do not reflect those of the Department of Veterans Affairs or any other agency of the USA Government. AUTHOR CONTRIBUTIONS: Conceptualization: SJF, MHF; data acquisition and analysis: LAS, SRR, MHF, EAU; writing, review and editing: MHF, SJF, LAS, SRR, EAU; funding acquisition: SJF, MHF, SRR; project supervision: SJF. All authors have read and agreed to the final submitted version of the manuscript. All authors agree to be accountable for the content of the work. FUNDING: Supported, in part, by U.S.P.H.S. (NIH) grants R01EY007361 (SJF), 1 UL1 TR001412 (to the University at Buffalo (SJF)), departmental laboratory start-up funds from the University at Buffalo (MHF), and by facilities and resources provided by the VA Western NY Healthcare System (MHF, SJF, SRR, LAS). SJF is the recipient of a Research Career Scientist Award (I K6 BX005787) from the Department of Veterans Affairs, BLR&D Service. SRR was the recipient of two Fight for Sight Summer Student Fellowships during the initial phase of this study, as well as a subsequent Fight for Sight Postdoctoral Award. SRR is the recipient of two Career Starter Research Grant Awards from the Knights Templar Eye Foundation, Inc. DATA AVAILABILITY STATEMENT The RNA-Seq data generated in this study have been deposited in the National Center for Biotechnology Information Gene Expression Omnibus (NCBI-GEO) database (GEO accession number GSE185028). iPSC-RPE cells derived in the course of the present study will be made available upon request.

REFERENCES

1. Yu H, Lee MH, Starck L, Elias ER, Irons M, Salen G, Patel SB, Tint GS. Spectrum of Delta [(7)]-dehydrocholesterol reductase mutations in patients with the Smith-Lemli-Opitz (RSH) syndrome. Hum Mol Genet 2000; 9:1385-91. .
2. Yu H, Patel SB. Recent insights into the Smith-Lemli-Opitz syndrome. Clin Genet 2005; 68:383-91. .
3. Witsch-Baumgartner M, Fitzky BU, Ogorelkova M, Kraft HG, Moebius FF, Glossmann H, Seedorf U, Gillessen-Kaesbach G, Hoffmann GF, Clayton P, Kelley RI, Utermann G. Mutational spectrum in the Delta7-sterol reductase gene and genotype-phenotype correlation in 84 patients with Smith-Lemli-Opitz syndrome. Am J Hum Genet 2000; 66:402-12. .
4. Tint GS, Irons M, Elias ER, Batta AK, Frieden R, Chen TS, Salen G. Defective cholesterol biosynthesis associated with the Smith-Lemli-Opitz syndrome. N Engl J Med 1994; 330:107-13. .
5. Shefer S, Salen G, Batta AK, Honda A, Tint GS, Irons M, Elias ER, Chen TC, Holick MF. Markedly inhibited 7-dehydrocholesterol-delta 7-reductase activity in liver microsomes from Smith-Lemli-Opitz homozygotes. J Clin Invest 1995; 96:1779-85. .
6. Yu H, Tint GS, Salen G, Patel SB. Detection of a common mutation in the RSH or Smith-Lemli-Opitz syndrome by a PCR-RFLP assay: IVS8-G→C is found in over sixty percent of US propositi. Am J Med Genet 2000; 90:347-50. .
7. Lazarin GA, Haque IS, Evans EA, Goldberg JD. Smith-Lemli-Opitz syndrome carrier frequency and estimates of in utero mortality rates. Prenat Diagn 2017; 37:350-5. .
8. Aneja A, Tierney E. Autism: the role of cholesterol in treatment. Int Rev Psychiatry 2008; 20:165-70. .
9. Diaz-Stransky A, Tierney E. Cognitive and behavioral aspects of Smith-Lemli-Opitz syndrome. Am J Med Genet C Semin Med Genet 2012; 160C:295-300. .
10. Elias ER, Hansen RM, Irons M, Quinn NB, Fulton AB. Rod photoreceptor responses in children with Smith-Lemli-Opitz syndrome. Arch Ophthalmol 2003; 121:1738-43. .
11. Garry D, Hansen RM, Moskowitz A, Elias ER, Irons M, Fulton AB. Cone ERG responses in patients with Smith-Lemli-Opitz Syndrome (SLOS). Doc Ophthalmol 2010; 121:85-91. .

12. Kretzer FL, Hittner HM, Mehta RS. Ocular manifestations of the Smith-Lemli-Opitz syndrome. Arch Ophthalmol 1981; 99:2000-6. .

13. Correa-Cerro LS, Wassif CA, Kratz L, Miller GF, Munasinghe JP, Grinberg A, Fliesler SJ, Porter FD. Development and characterization of a hypomorphic Smith-Lemli-Opitz syndrome mouse model and efficacy of simvastatin therapy. Hum Mol Genet 2006; 15:839-51. .

14. Marcos J, Shackleton CH, Buddhikot MM, Porter FD, Watson GL. Cholesterol biosynthesis from birth to adulthood in a mouse model for 7-dehydrosterol reductase deficiency (Smith-Lemli-Opitz syndrome). Steroids 2007; 72:802-8. .

15. Wassif CA, Zhu P, Kratz L, Krakowiak PA, Battaile KP, Weight FF, Grinberg A, Steiner RD, Nwokoro NA, Kelley RI, Stewart RR, Porter FD. Biochemical, phenotypic and neurophysiological characterization of a genetic mouse model of RSH/Smith–Lemli–Opitz syndrome. Hum Mol Genet 2001; 10:555-64. .

16. Kolf-Clauw M, Chevy F, Wolf C, Siliart B, Citadelle D, Roux C. Inhibition of 7-dehydrocholesterol reductase by the teratogen AY9944: a rat model for Smith-Lemli-Opitz syndrome. Teratology 1996; 54:115-25. .

17. Kolf-Clauw M, Chevy F, Siliart B, Wolf C, Mulliez N, Roux C. Cholesterol biosynthesis inhibited by BM15.766 induces holoprosencephaly in the rat. Teratology 1997; 56:188-200. .

18. Fliesler SJ, Peachey NS, Richards MJ, Nagel BA, Vaughan DK. Retinal degeneration in a rodent model of Smith-Lemli-Opitz syndrome: electrophysiologic, biochemical, and morphologic features. Arch Ophthalmol 2004; 122:1190-200. .

19. Ramachandra Rao S, Pfeffer BA, Mas Gomez N, Skelton LA, Keiko U, Sparrow JR, Rowsam AM, Mitchell CH, Fliesler SJ. Compromised phagosome maturation underlies RPE pathology in cell culture and whole animal models of Smith-Lemli-Opitz Syndrome. Autophagy 2018; 14:1-22. .

20. Francis KR, Ton AN, Xin Y, O'Halloran PE, Wassif CA, Malik N, Williams IM, Cluzeau CV, Trivedi NS, Pavan WJ, Cho W, Westphal H, Porter FD. Modeling Smith-Lemli-Opitz syndrome with induced pluripotent stem cells reveals a causal role for Wnt/beta-catenin defects in neuronal cholesterol synthesis phenotypes. Nat Med 2016; 22:388-96. .

21. Pfeffer BA. Improved methodology for cell culture of human and monkey retinal pigment epithelium. Prog Retinal Res 1991; 10:251-91. .

22. Pfeffer BA, Fliesler SJ. Streamlined duplex live-dead microplate assay for cultured cells. Exp Eye Res 2017; 161:17-29. .

23. Pfeffer BA, Xu L, Porter NA, Rao SR, Fliesler SJ. Differential cytotoxic effects of 7-dehydrocholesterol-derived oxysterols on cultured retina-derived cells: Dependence on sterol structure, cell type, and density. Exp Eye Res 2016; 145:297-316. .

24. Rak DJ, Hardy KM, Jaffe GJ, McKay BS. Ca++-switch induction of RPE differentiation. Exp Eye Res 2006; 82:648-56. .

25. Cham BE, Knowles BR. A solvent system for delipidation of plasma or serum without protein precipitation. J Lipid Res 1976; 17:176-81. .

26. Sievers F, Wilm A, Dineen D, Gibson TJ, Karplus K, Li W, Lopez R, McWilliam H, Remmert M, Soding J, Thompson JD, Higgins DG. Fast, scalable generation of high-quality protein multiple sequence alignments using Clustal Omega. Mol Syst Biol 2011; 7:539-.

27. Keller RK, Mitchell DA, Goulah CC, Fliesler SJ. Hepatic isoprenoid metabolism in a rat model of Smith-Lemli-Opitz Syndrome. Lipids 2013; 48:219-29. .

28. Ramachandra Rao S, Skelton LA, Wu F, Onysk A, Spolnik G, Danikiewicz W, Butler MC, Stacks DA, Surmacz L, Mu X, Swiezewska E, Pittler SJ, Fliesler SJ. Retinal Degeneration Caused by Rod-Specific Dhdds Ablation Occurs without Concomitant Inhibition of Protein N-Glycosylation. iScience 2020; 23:101198.

29. Tyner C, Barber GP, Casper J, Clawson H, Diekhans M, Eisenhart C, Fischer CM, Gibson D, Gonzalez JN, Guruvadoo L, Haeussler M, Heitner S, Hinrichs AS, Karolchik D, Lee BT, Lee CM, Nejad P, Raney BJ, Rosenbloom KR, Speir ML, Villarreal C, Vivian J, Zweig AS, Haussler D, Kuhn RM, Kent WJ. The UCSC Genome Browser database: 2017 update. Nucleic Acids Res 2017; 45:D1D626-34. .

30. Liao Y, Smyth GK, Shi W. The R package Rsubread is easier, faster, cheaper and better for alignment and quantification of RNA sequencing reads. Nucleic Acids Res 2019; 47:e47-.

31. Au ED, Fernandez-Godino R, Kaczynksi TJ, Sousa ME, Farkas MH. Characterization of lincRNA expression in the human retinal pigment epithelium and differentiated induced pluripotent stem cells. PLoS One 2017; 12:e0183939-.

32. Muller C, Charniga C, Temple S, Finnemann SC. Quantified F-Actin Morphology Is Predictive of Phagocytic Capacity of Stem Cell-Derived Retinal Pigment Epithelium. Stem Cell Reports 2018; 10:1075-87. .

33. Phillips BE, Cancel L, Tarbell JM, Antonetti DA. Occludin independently regulates permeability under hydrostatic pressure and cell division in retinal pigment epithelial cells. Invest Ophthalmol Vis Sci 2008; 49:2568-76. .

34. Benedicto I, Lehmann GL, Ginsberg M, Nolan DJ, Bareja R, Elemento O, Salfati Z, Alam NM, Prusky GT, Llanos P, Rabbany SY, Maminishkis A, Miller SS, Rafii S, Rodriguez-Boulan E. Concerted regulation of retinal pigment epithelium basement membrane and barrier function by angiocrine factors. Nat Commun 2017; 8:15374-.

35. Li CL, Yang D, Cao X, Wang F, Hong DY, Wang J, Shen XC, Chen Y. Fibronectin induces epithelial-mesenchymal transition in human breast cancer MCF-7 cells via activation of calpain. Oncol Lett 2017; 13:3889-95. .

36. Yang Z, Zhang X, Gang H, Li X, Li Z, Wang T, Han J, Luo T, Wen F, Wu X. Up-regulation of gastric cancer cell invasion by Twist is accompanied by N-cadherin and fibronectin expression. Biochem Biophys Res Commun 2007; 358:925-30. .

37. Frankish A, Diekhans M, Jungreis I, Lagarde J, Loveland JE, Mudge JM, Sisu C, Wright JC, Armstrong J, Barnes I, Berry A, Bignell A, Boix C, Carbonell Sala S, Cunningham F, Di Domenico T, Donaldson S, Fiddes IT, Garcia Giron C,

Gonzalez JM, Grego T, Hardy M, Hourlier T, Howe KL, Hunt T, Izuogu OG, Johnson R, Martin FJ, Martinez L, Mohanan S, Muir P, Navarro FCP, Parker A, Pei B, Pozo F, Riera FC, Ruffier M, Schmitt BM, Stapleton E, Suner MM, Sycheva I, Uszczynska-Ratajczak B, Wolf MY, Xu J, Yang YT, Yates A, Zerbino D, Zhang Y, Choudhary JS, Gerstein M, Guigo R, Hubbard TJP, Kellis M, Paten B, Tress ML, Flicek P. Gencode 2021. Nucleic Acids Res 2021; 49:D1D916-23. .

38. Li Y, Ge X, Peng F, Li W, Li JJ. Exaggerated false positives by popular differential expression methods when analyzing human population samples. Genome Biol 2022; 23:79-.

39. Wu S, Du Y, Beckford J, Alachkar H. Upregulation of the EMT marker vimentin is associated with poor clinical outcome in acute myeloid leukemia. J Transl Med 2018; 16:170-.

40. Liggett TE, Griffiths TD, Gaillard ER. Isolation and characterization of a spontaneously immortalized bovine retinal pigmented epithelial cell line. BMC Cell Biol 2009; 10:33-.

41. Hunt RC, Davis AA. Altered expression of keratin and vimentin in human retinal pigment epithelial cells in vivo and in vitro. J Cell Physiol 1990; 145:187-99. .

42. Honke K, Wada Y. Regulation of vimentin expression and protease-mediated vimentin degradation during differentiation of human monocytic leukemia cells. Jpn J Cancer Res 1997; 88:484-91. .

43. Nelson WJ, Traub P. Proteolysis of vimentin and desmin by the Ca2+-activated proteinase specific for these intermediate filament proteins. Mol Cell Biol 1983; 3:1146-56. .

44. Liao JL, Yu J, Huang K, Hu J, Diemer T, Ma Z, Dvash T, Yang XJ, Travis GH, Williams DS, Bok D, Fan G. Molecular signature of primary retinal pigment epithelium and stem-cell-derived RPE cells. Hum Mol Genet 2010; 19:4229-38. .

45. Ramachandra Rao S, Fliesler SJ. Cholesterol homeostasis in the vertebrate retina: biology and pathobiology. J Lipid Res 2021; 62:100057-.

46. Lyssenko NN, Haider N, Picataggi A, Cipollari E, Jiao W, Phillips MC, Rader DJ, Chavali VRM. Directional ABCA1-mediated cholesterol efflux and apoB-lipoprotein secretion in the retinal pigment epithelium. J Lipid Res 2018; 59:1927-39. .

47. Wassif CA, Vied D, Tsokos M, Connor WE, Steiner RD, Porter FD. Cholesterol storage defect in RSH/Smith-Lemli-Opitz syndrome fibroblasts. Mol Genet Metab 2002; 75:325-34. .

48. Fliesler SJ, Peachey NS, Herron J, Hines KM, Weinstock NI, Ramachandra Rao S, Xu L. Prevention of Retinal Degeneration in a Rat Model of Smith-Lemli-Opitz Syndrome. Sci Rep 2018; 8:1286-.

49. Sripathi SR, Hu MW, Liu MM, Wan J, Cheng J, Duan Y, Mertz JL, Wahlin KJ, Maruotti J, Berlinicke CA, Qian J, Zack DJ. Transcriptome Landscape of Epithelial to Mesenchymal Transition of Human Stem Cell-Derived RPE. Invest Ophthalmol Vis Sci 2021; 62:1-.

50. Sripathi SR, Hu MW, Turaga RC, Mertz J, Liu MM, Wan J, Maruotti J, Wahlin KJ, Berlinicke CA, Qian J, Zack DJ. Proteome Landscape of Epithelial-to-Mesenchymal Transition (EMT) of Retinal Pigment Epithelium Shares Commonalities With Malignancy-Associated EMT. Mol Cell Proteomics 2021; 20:100131-.

51. Boles NC, Fernandes M, Swigut T, Srinivasan R, Schiff L, Rada-Iglesias A, Wang Q, Saini JS, Kiehl T, Stern JH, Wysocka J, Blenkinsop TA, Temple S. Epigenomic and Transcriptomic Changes During Human RPE EMT in a Stem Cell Model of Epiretinal Membrane Pathogenesis and Prevention by Nicotinamide. Stem Cell Reports 2020; 14:631-47. .

52. Xu L, Korade Z, Porter NA. Oxysterols from free radical chain oxidation of 7-dehydrocholesterol: product and mechanistic studies. J Am Chem Soc 2010; 132:2222-32. .

53. Pfeffer BA, Xu L, Fliesler SJ. Transcriptomic Changes Associated with Loss of Cell Viability Induced by Oxysterol Treatment of a Retinal Photoreceptor-Derived Cell Line: An In Vitro Model of Smith-Lemli-Opitz Syndrome. Int J Mol Sci 2021; 22:2339

54. Singh R, Phillips MJ, Kuai D, Meyer J, Martin JM, Smith MA, Perez ET, Shen W, Wallace KA, Capowski EE, Wright LS, Gamm DM. Functional analysis of serially expanded human iPS cell-derived RPE cultures. Invest Ophthalmol Vis Sci 2013; 54:6767-78. .

55. Feng Q, Lu SJ, Klimanskaya I, Gomes I, Kim D, Chung Y, Honig GR, Kim KS, Lanza R. Hemangioblastic derivatives from human induced pluripotent stem cells exhibit limited expansion and early senescence. Stem Cells 2010; 28:704-12. .

56. Croze RH, Buchholz DE, Radeke MJ, Thi WJ, Hu Q, Coffey PJ, Clegg DO. ROCK Inhibition Extends Passage of Pluripotent Stem Cell-Derived Retinal Pigmented Epithelium. Stem Cells Transl Med 2014; 3:1066-78. .

57. Tamiya S, Liu L, Kaplan HJ. Epithelial-mesenchymal transition and proliferation of retinal pigment epithelial cells initiated upon loss of cell-cell contact. Invest Ophthalmol Vis Sci 2010; 51:2755-63. .

58. Kalluri R, Weinberg RA. The basics of epithelial-mesenchymal transition. J Clin Invest 2009; 119:1420-8. .

59. Yang J, Antin P, Berx G, Blanpain C, Brabletz T, Bronner M, Campbell K, Cano A, Casanova J, Christofori G, Dedhar S, Derynck R, Ford HL, Fuxe J, Garcia de Herreros A, Goodall GJ, Hadjantonakis AK, Huang RYJ, Kalcheim C, Kalluri R, Kang Y, Khew-Goodall Y, Levine H, Liu J, Longmore GD, Mani SA, Massague J, Mayor R, McClay D, Mostov KE, Newgreen DF, Nieto MA, Puisieux A, Runyan R, Savagner P, Stanger B, Stemmler MP, Takahashi Y, Takeichi M, Theveneau E, Thiery JP, Thompson EW, Weinberg RA, Williams ED, Xing J, Zhou BP, Sheng G, Association EMTI. Guidelines and definitions for research on epithelial-mesenchymal transition. Nat Rev Mol Cell Biol 2020; 21:341-52. .

60. Haynes J, Srivastava J, Madson N, Wittmann T, Barber DL. Dynamic actin remodeling during epithelial-mesenchymal transition depends on increased moesin expression. Mol Biol Cell 2011; 22:4750-64. .

61. Bharti K, den Hollander AI, Lakkaraju A, Sinha D, Williams DS, Finnemann SC, Bowes-Rickman C, Malek G, D'Amore

PA. Cell culture models to study retinal pigment epithelium-related pathogenesis in age-related macular degeneration. Exp Eye Res 2022; 222:109170-.